Chemical Science

ROYAL SOCIETY OF CHEMISTRY

EDGE ARTICLE

View Article Online
View Journal | View Issue

Cite this: *Chem. Sci.*, 2025, **16**, 17911

All publication charges for this article have been paid for by the Royal Society of Chemistry

High-entropy metal phosphide nanoparticles for accelerated lithium polysulfide conversion

Manchuan Guo,† Jin Guo,† Tao Ren, Haici Deng, Yanqiu Zhu and Jinliang Zhu *

To overcome the persistent challenges of sluggish lithium polysulfide (LiPS) conversion kinetics and the shuttle effect in Li–S batteries, this work introduces a novel, cost-effective thermal treatment strategy for synthesizing high-entropy metal phosphide catalysts using cation-bonded phosphate resins. For the first time, we successfully fabricated single-phase high-entropy $Fe_{0.20}Co_{0.62}Ni_{0.14}Cu_{0.23}Mn_{0.38}P$ nanoparticles anchored on a porous carbon network (HEP/C). HEP/C demonstrates enhanced electronic conductivity and superior LiPS adsorption capability, substantially accelerating its redox kinetics. These catalytic improvements arise from (1) synergistic electronic modulation by the five constituent metals, which elevates d-band electron energy levels, and (2) lattice distortion induced by atomic radius mismatches, collectively generating a dense array of highly active catalytic sites. The HEP/C@S cathode delivers an ultrahigh initial specific capacity of 1402.18 mA h g^{-1} at 0.2C, outstanding cycling stability with merely 0.05% capacity decay per cycle over 1000 cycles at 5C, and a remarkable initial energy density of 455 Wh kg^{-1} in practical pouch cells. This work not only presents an efficient synthesis strategy for high-entropy materials but also provides fundamental insights into the design principles of advanced LiPS conversion catalysts for high-performance Li–S batteries.

Received 23rd June 2025
Accepted 30th August 2025

DOI: 10.1039/d5sc04604a

rsc.li/chemical-science

1 Introduction

Lithium–sulfur (Li–S) batteries have emerged as a promising next-generation energy storage technology, owing to their ultrahigh theoretical specific capacity, exceptional energy density, and the inherent advantages of sulfur cathodes—low cost, natural abundance, and environmental benignity.[1,2] However, the practical application of Li–S batteries is hindered by several critical challenges, including sluggish redox kinetics of lithium polysulfides (LiPSs) and their shuttle.[3] Soluble LiPSs migrate between electrodes, leading to rapid capacity decay and diminished coulombic efficiency.[4] To mitigate these issues, the rational design of electrocatalysts to accelerate soluble LiPS conversion into insoluble Li_2S has been widely recognized as an effective strategy.[5,6]

In this context, high-entropy materials have recently garnered considerable attention as advanced electrocatalysts for sulfur redox reactions. These materials consist of five or more metal elements, offering abundant active sites, tunable electronic configurations, and exceptional stability—properties that are highly desirable for complex electrochemical processes.[7] Among various high-entropy materials,[8] high-entropy sulfides[9] often face thermodynamic instability and structural deformation under strong redox conditions. High-entropy oxides[10] suffer from inherently poor electrical conductivity and limited ion diffusion within their lattice. And high-entropy carbides[11] exhibit weak ability to anchor and confine LiPS shuttling. Only high-entropy metal phosphides stand out due to their superior electrical conductivity, high catalytic activity, and robust structural stability, making them ideal candidates for facilitating sulfur redox kinetics. For instance, Gao *et al.* developed $Pd_{0.34}Sn_{0.15}Ni_{0.05}Co_{0.09}Cu_{0.29}P_{0.08}$ nanoparticles anchored on fluorinated activated carbon, where the synergistic interplay of Pd (high activity), Cu (conductivity), and Co/Ni (cost-effective cocatalysts) significantly enhanced LiPS conversion.[12] Similarly, Wang *et al.* designed a NiCoMnFeCrP catalyst that stabilized reactive $S^{3\bullet-}$ intermediates, enabling efficient LiPS conversion across a wide temperature range with exceptional cycling stability.[13]

Despite these advances, the synthesis of high-entropy phosphides remains challenging. Current methods can be broadly categorized into one-step (*e.g.*, colloidal synthesis,[14] solvothermal reactions,[15] and mechanochemical ball milling[16]) and two-step approaches (*e.g.*, precursor phosphidation[17–19]). For instance, Park *et al.*[16] employed high-energy mechanical ball milling to reconfigure bulk precursor materials at the extreme temperatures and under the extreme pressures generated during collision events. This one-step method provides a straightforward route for synthesizing high-entropy

School of Resources, Environment and Materials, Guangxi Key Laboratory of Processing for Non-ferrous Metals and Featured Materials, Guangxi University, Nanning 530004, P. R. China. E-mail: jlzhu85@163.com; jlzhu@gxu.edu.cn

† These authors contributed equally to this work.

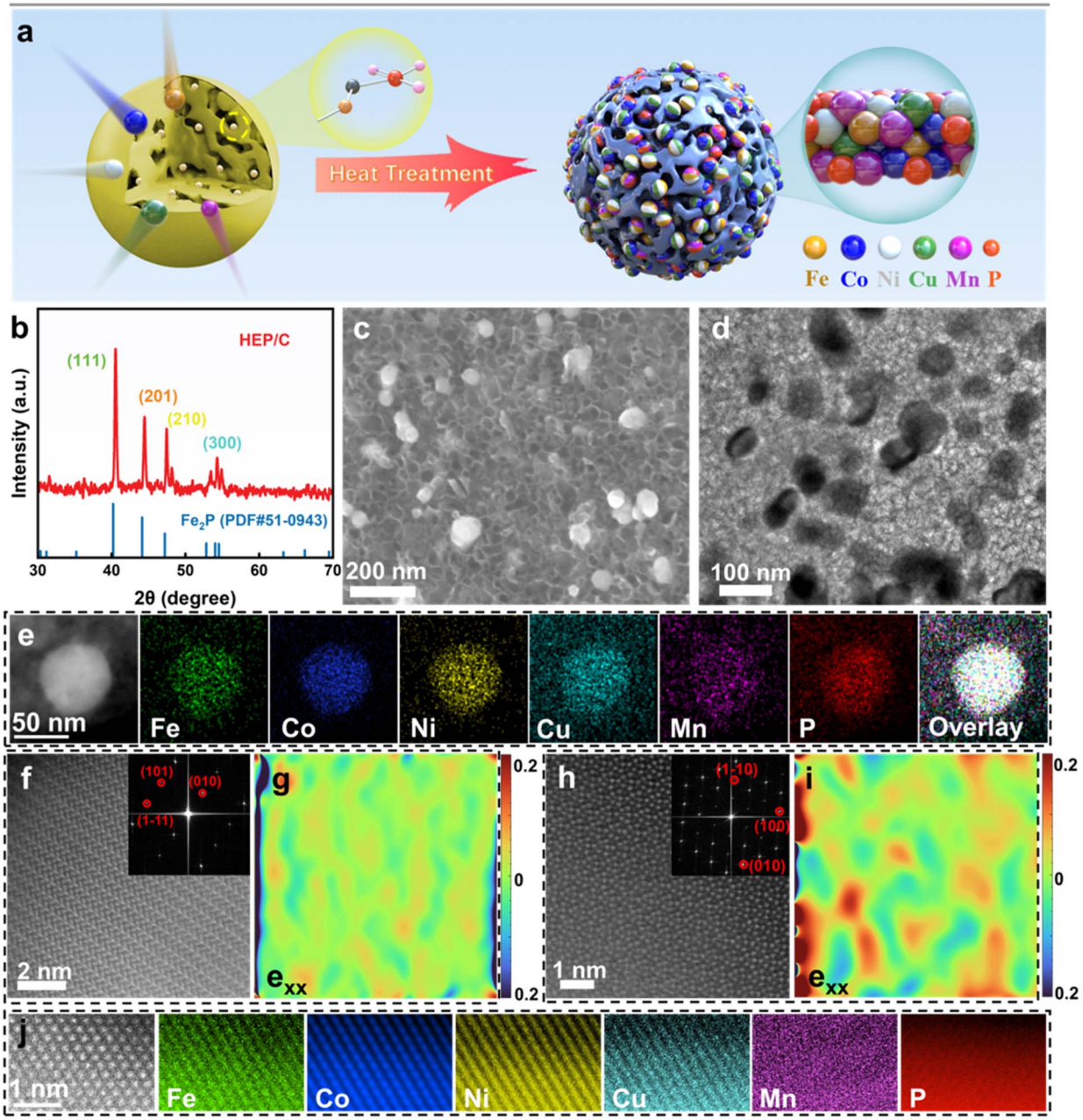

Fig. 1 (a) Schematic illustration of the synthesis mechanism for HEP/C. (b) XRD pattern, (c) SEM image, and (d) TEM image of the as-prepared HEP/C. (e) HAADF image and corresponding EDS element mapping of HEP/C. (f) and (h) STEM image viewed along the [−101] and [001] zone axis and (g) and (i) corresponding strain distribution maps. (j) Atomic-resolution elemental mapping of HEP/C.

phosphides such as $ZnCuGaGeSiP_5$. However, despite its simplicity, this approach often results in inhomogeneous reactions, unintended impurity phases, and limited control over reaction kinetics. In contrast, two-step synthesis strategies offer greater morphological control. For example, Geng *et al.*[19] first hydrothermally treated nickel foam with a solution containing Ni, Fe, Cr, Co, and Ag nitrates, along with urea and ammonium fluoride, in a high-pressure autoclave. Subsequently, they subjected the intermediate product to phosphorization using NaH_2PO_2 in a tube furnace, ultimately obtaining dendritic NiFeCrCoAgP. While this method enables precise tuning of the phosphide's microstructure, it encounters challenges in achieving complete and uniform phosphorization, particularly within the material's bulk regions.

Herein, we present a novel and scalable synthesis strategy for high-entropy metal phosphides *via* thermally induced transformation of cation-bonded phosphate resin. By leveraging ionic bonds to precisely incorporate metal cations (Fe, Co, Ni, Cu, and Mn) into a phosphorus-rich resin framework, followed by controlled thermal treatment, we successfully fabricated single-phase $Fe_{0.20}Co_{0.62}Ni_{0.14}Cu_{0.23}Mn_{0.38}P$ nanoparticles uniformly dispersed on a porous carbon (HEP/C; Fig. 1a). This

approach not only ensures atomic-level homogeneity and tunable metal stoichiometry but also simplifies the synthesis process while reducing costs. Theoretical and experimental analyses reveal that the multi-metallic synergy in HEP/C modulates the electronic structure of the catalyst, enhancing charge transfer and creating lattice distortions that expose additional active sites. Consequently, HEP/C exhibits outstanding catalytic activity for LiPS conversion, enabling Li–S pouch cells with a high energy density of 455 Wh kg^{-1}. This work underscores the potential of high-entropy phosphides as high-performance, commercially viable catalysts for advanced Li–S batteries.

2 Results and discussion

2.1 Synthesis and characterization

The $Fe_{0.20}Co_{0.62}Ni_{0.14}Cu_{0.23}Mn_{0.38}P$ nanoparticles anchored on a porous carbon network (HEP/C) were synthesized *via* a one-step thermal treatment of cation (Fe^{3+}, Co^{2+}, Ni^{2+}, Cu^{2+} and Mn^{2+})-bonded phosphate resin, as illustrated in Fig. 1a. XRD analysis (Fig. 1b) confirmed the formation of a high-entropy phosphide phase, with characteristic peaks at 40.5°, 44.5°, 47.5°, and 54.3° corresponding to the (111), (201), (210), and (300) planes of Fe_2P (JCPDS no. 51-0943), respectively. Notably, compared to pristine Fe_2P, these peaks exhibit a slight shift toward higher diffraction angles, which can be attributed to the lattice contraction caused by partial substitution of Fe with smaller Co, Ni, and Cu atoms. Additionally, the broadening of these peaks is due to the scattering of diffraction signals resulting from local atomic disorder.[20] This observation aligns with the formation of a solid-solution structure, where the incorporation of multiple metal species modifies the host lattice parameters.

Scanning electron microscopy (SEM) imaging (Fig. 1c) revealed a homogeneous distribution of HEP nanoparticles (~50 nm in diameter) embedded within the porous carbon. Transmission electron microscopy (TEM) further corroborated this morphology, showing well-dispersed nanoparticles with an average size of 54.6 nm (Fig. 1d, size distribution in Fig. S1). Energy dispersive spectrometry (EDS) elemental mapping (Fig. 1e) confirmed the uniform spatial distribution of all five transition metals (Fe, Co, Ni, Cu, and Mn) and phosphorus across the HEP/C composite, highlighting the successful formation of a high-entropy phase with atomic-level homogeneity. Such structural uniformity is critical for maximizing active site exposure and facilitating efficient LiPS adsorption and conversion. For comparison, $Fe_{0.38}Co_{0.75}Ni_{0.20}Cu_{0.36}P$/C (MEP/C), Fe_2P/C and Mn_2P/C were also synthesized, exhibiting diffraction patterns consistent with those of Fe_2P (JCPDS no. 51-0943), Fe_2P (JCPDS no. 51-0943) and Mn_2P (JCPDS no. 89-2741). And the surface morphology and particle size of MEP/C, Fe_2P/C, and Mn_2P/C are essentially consistent with those of HEP/C (Fig. S2–S4).

X-ray photoelectron spectroscopy (XPS) analysis of HEP/C confirmed the presence of Fe, Co, Ni, Cu, Mn, and P. As shown in Fig. S5a, the Fe 2p spectrum exhibits characteristic peaks at 712.46 and 725.26 eV, corresponding to $Fe^{\delta+}$, while the peaks at 706.50 and 722.67 eV are assigned to the Fe–P bond.[21] Similarly, in the Co 2p spectrum (Fig. S5b), the peaks at 782.06 and 797.85 eV are attributed to $Co^{\delta+}$, whereas those at 779.14 and 794.14 eV arise from the Co–P bond.[22] The Ni 2p spectrum (Fig. S5c) displays $Ni^{\delta+}$ states at 857.60 and 875.43 eV, alongside Ni–P contributions at 853.33 and 870.50 eV.[23] For Cu 2p (Fig. S5d), the peaks at 934.63 and 954.49 eV correspond to $Cu^{\delta+}$, while those at 932.84 and 952.69 eV are indicative of Cu–P bonding.[24] The Mn 2p spectrum (Fig. S5e) reveals $Mn^{\delta+}$ signals at 641.76 and 650.41 eV, with an additional peak at 638.67 eV assigned to Mn–P.[25] In the P 2p spectrum (Fig. S5f), the peaks at 132.35 and 133.30 eV are attributed to P–C and P–O bonds, respectively, while the signal at 129.06 eV corresponds to metal phosphides (P–M, where M = Fe, Co, Ni, Cu, Mn).[26] The relatively weak intensity of the P–M peak can be attributed to the carbon matrix in HEP/C, which may partially obscure the phosphide signal.

Aberration-corrected STEM imaging (Fig. 1f and h) resolved the atomic arrangement of HEP nanoparticles, revealing distinct crystallographic orientations with exposed (101), (010), and (1−11) facets (FFT inset). The hexagonal Fe_2P structure was further evidenced by diffraction spots corresponding to (1−10), (100), and (010) planes. Geometric phase analysis of the atomic-resolution images (Fig. 1g and i) unveiled significant stress–strain distribution along the e_{xx} direction, with compressive (blue-yellow) and tensile (yellow-red) regions localized at the nanoparticle surface. In Fig. 1g, a 0.1% tensile strain is observed along the indicated direction, and Fig. 1i reveals a 0.2% tensile strain and a 0.1% compressive strain in the corresponding orientation. This strain originates from lattice distortions caused by the incorporation of heterometallic atoms with varying atomic radius (*e.g.*, Cu (1.27 Å) *vs.* Mn (1.36 Å)), which locally perturb the Fe_2P framework while maintaining its overall crystallinity.[27,28] Such strain engineering offers three key advantages: diverse LiPS binding sites, enhanced catalytic activity and improved Li^+ transport. Varied lattice spacings create tailored chemical environments for adsorbing both long- and short-chain LiPSs. Strain-induced electron redistribution exposes additional active sites for sulfur redox reactions. Modified energy landscapes facilitate Li^+ diffusion pathways. Atomically resolved EDS mapping (Fig. 1j) conclusively demonstrates the homogeneous distribution of all five transition metals (Fe, Co, Ni, Cu, and Mn) and phosphorus throughout the nanoparticles, with no observable phase segregation or elemental clustering. This atomic-level mixing, combined with the engineered lattice strain, synergistically enhances both the adsorption and conversion kinetics of LiPSs.

2.2 Adsorption towards LiPSs and theoretical analysis

As illustrated in Fig. 2a and S6, Li_2S_6 was employed as a representative soluble LiPS to evaluate the adsorption capacities of various catalysts.[29] Following a 3-hour adsorption period, only the solution containing HEP/C became completely clear and transparent, while the others retained a faint yellow tint. Notably, the solution with Mn_2P exhibited the lightest coloration, whereas those with MEP/C and Fe_2P/C showed more

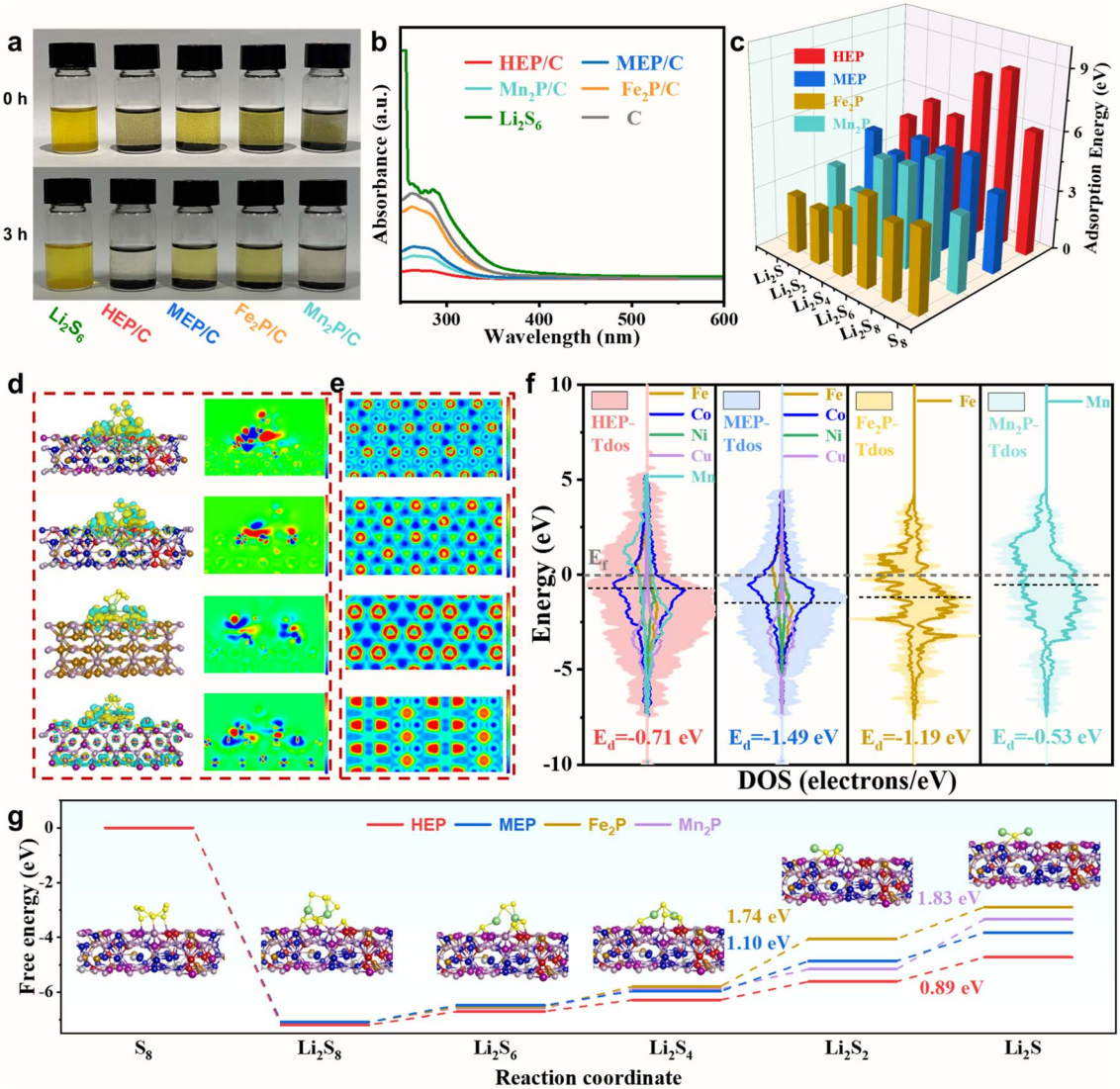

Fig. 2 (a) Visual comparison of Li_2S_6 solution adsorption and (b) corresponding UV-vis spectra quantifying polysulfide concentration changes after 3 h by different catalysts. (c) DFT-calculated adsorption energies of various LiPSs and S_8 on different crystal surfaces. (d) Differential charge density distributions and 2D cross-sections showing Li_2S_6 adsorption configurations. (e) 3D charge density slices, (f) DOS profiles and (g) Gibbs free energy of HEP, MEP, Fe_2P and Mn_2P.

intense yellow hues and the porous carbon exhibits the deepest yellow color. To quantify the residual Li_2S_6 concentrations, UV-vis spectroscopy was performed on the supernatants (Fig. 2b). A prominent absorption peak at 265 nm confirmed the presence of Li_2S_6.[30] HEP/C displayed significantly lower absorbance compared to Mn_2P/C, MEP/C, Fe_2P/C and C, indicating that incorporating HEP into C materials with poor LiPS adsorption capability significantly enhances their anchoring ability for LiPSs.

Density functional theory (DFT) calculations were performed to assess the adsorption energies of LiPSs on the (002) surfaces of HEP, MEP, and Fe_2P, as well as the (210) surface of Mn_2P (optimized adsorption configurations in Fig. S7–S10). The adsorption energy histogram (Fig. 2c) revealed that HEP (002) exhibited the strongest binding, followed by Mn_2P (210) and MEP (002), while Fe_2P (002) displayed the weakest interaction. Differential charge density analysis of Li_2S_6 adsorbed on these surfaces (Fig. 2d) highlighted electron accumulation (yellow) and depletion (blue) regions. The Li_2S_6–HEP (002) interface exhibited the most pronounced electron exchange, indicating robust chemical bonding between the HEP metal sites and Li_2S_6 sulfur atoms. These findings corroborate the visual adsorption and UV-vis results, confirming HEP's superior polysulfide anchoring ability. The strong adsorption of LiPSs on HEP (002) arises from covalent interactions with polysulfide sulfur atoms, enhancing interfacial electron/ion transfer and reducing the energy barrier for polysulfide conversion. This intimate contact further facilitates rapid S–S bond cleavage and reformation, promoting an efficient catalytic cycle. Collectively, these effects accelerate LiPS conversion kinetics and mitigate the shuttle effect.

To elucidate the distribution of metal active sites and their synergistic mechanisms, we computed the electron localization function (ELF, Fig. 2e) and density of states (DOS, Fig. 2f) using VASP. In the ELF map, red regions denote P atoms with localized electrons, while blue areas represent electron-deficient metal sites. Fe_2P and Mn_2P surfaces exhibited sparse metallic sites, whereas MEP showed uniform electron distribution across Fe, Co, Ni, and Cu sites. In contrast, HEP featured a higher abundance and diversity of metallic active sites. This heterogeneity enables selective adsorption and activation of intermediate species, lowering reaction energy barriers and facilitating multi-step LiPS conversion.[31,32]

Fig. 2f presents the total density of states (TDOS) for different catalysts along with the partial density of states (PDOS) of their constituent elements, with corresponding enlarged profiles shown in Fig. S11. Analysis reveals that in HEP, the electronic states near the Fermi level are dominated by d-orbital contributions from metallic components, suggesting superior electrical conductivity. The electronic structure of HEP results from synergistic interactions among Fe, Co, Ni, Cu, and Mn. Notably, HEP exhibits a higher d-band center (−0.71 eV) compared to MEP, which we attribute primarily to partial occupation of Mn 3d orbitals that introduces additional electronic states near the Fermi level. The incorporation of Mn serves dual functions: (1) it increases the configurational entropy of the HEP system, promoting electronic structure disorder and delocalization; (2) it strengthens d–p orbital hybridization between metal elements and phosphorus, collectively shifting the d-band center to higher energies. This distinctive electronic configuration simultaneously enhances LiPS adsorption strength and charge transport properties. By anchoring LiPS molecules at these active sites, HEP effectively concentrates reactants in the vicinity of the catalytic centers, thereby accelerating the redox reaction kinetics. This localized enrichment of LiPS not only reduces the diffusion distance for intermediates but also minimizes their shuttle effect, a critical factor in stabilizing the reaction system. Furthermore, HEP established a low-resistance pathway for electron transfer during LiPS conversion due to its rapid charge transport capabilities. This enables the swift reduction of long-chain LiPS (*e.g.*, Li_2S_4) to shorter, less soluble species (*e.g.*, Li_2S_2 and Li_2S), which are then stabilized on the HEP surface. The combined effects of enhanced adsorption and accelerated electron transfer can significantly lower the overall energy barrier for the reaction.[33] In contrast, MEP demonstrates a downward-shifted d-band center relative to base-phase Fe_2P due to the electronic structure modulation induced by Co, Ni, and Cu incorporation. Nevertheless, the multi-metallic composition broadens the Fermi-level electronic state distribution and increases total electron density, thereby improving electrical conductivity. While Mn_2P exhibits a relatively high d-band center (−0.53 eV) that facilitates LiPS adsorption,[34,35] its comparatively low electron density limits efficient charge transfer during LiPS conversion reactions, ultimately hindering rapid polysulfide transformation.

To further clarify the specific mechanism of HEP catalyzing LiPS conversion, we calculated the Gibbs free energy changes (ΔG) during the reduction processes of LiPSs (Fig. 2g). The ΔG values of rate-determining steps for various catalysts are labeled with numerical tags. The Gibbs free energy changes for HEP during the transformation of Li_2S_4 into Li_2S_2 and Li_2S are significantly lower than those of MEP, Fe_2P and Mn_2P, indicating that HEP accelerates liquid–solid reaction kinetics by reducing the energy barrier. This improvement is mainly attributed to moderate adsorption capacity and the multiple metal active sites of HEP, which provide a favorable local chemical environment for LiPS conversion, while Mn_2P exhibits the highest energy barrier during the critical step of Li_2S_2 conversion to Li_2S. This high energy barrier indicates that the nucleation and growth of Li_2S on the Mn_2P surface are significantly hindered, leading to a slow and incomplete transformation of LiPSs.

2.3 Electrocatalytic behavior of the catalysts

To systematically evaluate the catalytic performance for LiPS conversion under practical operating conditions, we assembled symmetric cells employing Li_2S_6 electrolyte. Cyclic voltammetry (CV) measurements were conducted at a scan rate of 1 mV s^{-1} to characterize the electrochemical behavior. As shown in Fig. 3a, the HEP/C-based cell demonstrated superior electrochemical activity, manifested by both the highest response current density and a well-defined pair of redox peaks. Notably, the peak-to-peak separation (ΔE) was remarkably small (89.8 mV), suggesting exceptionally fast redox kinetics and thorough LiPS catalytic conversion. These observations strongly indicate that HEP/C not only possesses excellent LiPS adsorption properties but also provides abundant active sites that facilitate efficient LiPS conversion during electrochemical cycling. In contrast, MEP/C, Fe_2P/C, and Mn_2P/C exhibited significantly lower current responses and less pronounced redox features, which we attribute to either limited LiPS adsorption capacity or inferior electrical conductivity, ultimately leading to their diminished catalytic performance.

To investigate the electrocatalytic behavior of HEP/C in LiPS redox reactions, a three-electrode system was employed, consisting of a glassy carbon rotating disk electrode (working electrode), lithium foil (counter/reference electrode), and an ether-based electrolyte containing 4 mM S_8. Linear sweep voltammetry (LSV) revealed distinct S-shaped polarization curves for all catalysts (Fig. 3b), signifying that LiPS conversion is governed by a combination of kinetic and diffusion control mechanisms across different potential ranges.[36,37] At high overpotentials (2.6 V), where the reduction of S_8 to Li_2S_8 (a two-electron process) is kinetically controlled, HEP/C exhibited both a higher onset potential and greater current density than MEP/C, Fe_2P/C, and Mn_2P/C. This suggests reduced reaction overpotential and faster reaction kinetics, likely due to the increased density of active sites on HEP/C that effectively adsorb and activate S_8 for subsequent conversion. Conversely, at lower overpotentials (2.05 V), the process shifts toward diffusion-controlled Li_2S_4 reduction to Li_2S_2/Li_2S. Here, HEP/C displayed the highest diffusion-limited current, confirming its superior electrocatalytic effect in promoting the liquid-to-solid phase transition of LiPSs—a critical feature for mitigating the

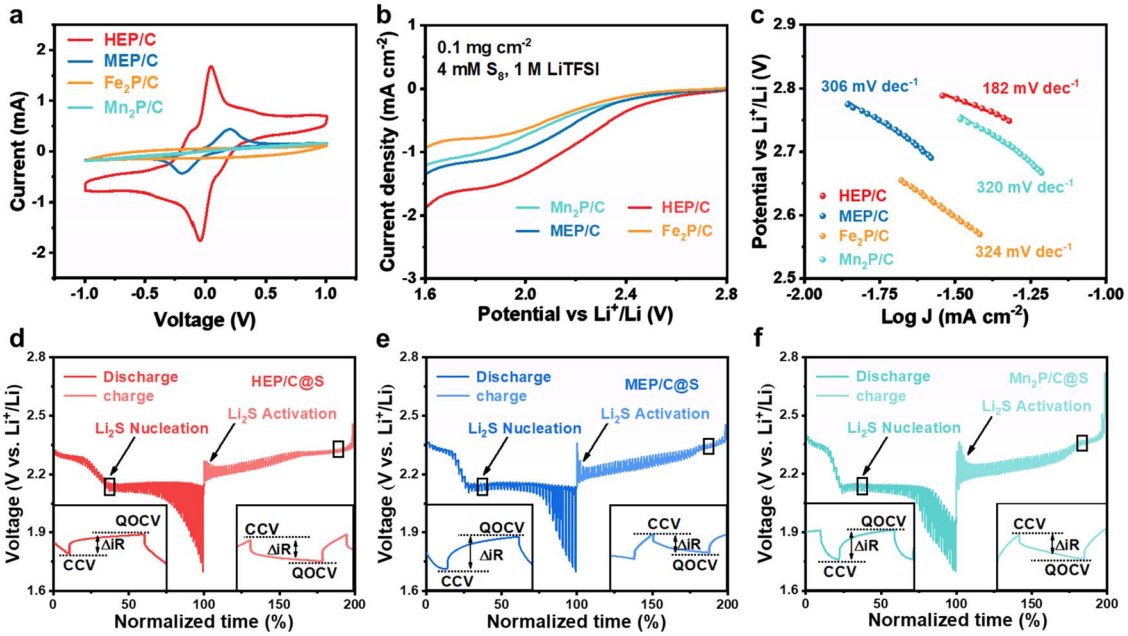

Fig. 3 (a) CV profiles of symmetric cells at a 1 mV s^{-1} scan rate. (b) LSV curves for sulfur reduction reaction activity comparison. (c) Tafel plots derived from LSV data. (d)–(f) GITT voltage profiles demonstrating (d) HEP/C, (e) MEP/C, and (f) Mn_2P/C.

shuttle effect. Further kinetic analysis *via* Tafel slopes in the mixed-control regime revealed that HEP/C achieves the lowest value (182 mV dec^{-1}), significantly outperforming MEP/C (306 mV dec^{-1}), Fe_2P/C (324 mV dec^{-1}), and Mn_2P/C (320 mV dec^{-1}) (Fig. 3c). This underscores HEP/C's exceptional ability to accelerate LiPS redox kinetics. Collectively, these results demonstrate that outstanding electrocatalytic performance of HEP/C stems from its optimized electronic structure, abundant active sites, and favorable interfacial chemistry, which collectively enhance LiPS adsorption, electron transfer, and reaction dynamics.

To further assess the electrocatalytic efficacy of different materials in facilitating Li_2S nucleation and activation, galvanostatic intermittent titration technique (GITT) measurements were performed at 0.05C on Li–S coin cells by employing HEP/C@S, MEP/C@S, Fe_2P/C@S, and Mn_2P/C@S as cathodes. The voltage difference (ΔiR) between the quasi-open-circuit voltage (QOCV) and the closed-circuit voltage (CCV) serves as a key indicator of internal resistance, providing insights into the polarization behavior in varying catalytic environments. As illustrated in Fig. 3d–f and S12, HEP/C@S demonstrates a significantly smaller ΔiR compared to MEP/C@S, Fe_2P/C@S, and Mn_2P/C@S. This reduced polarization underscores HEP/C@S's superior ability to enhance ion transport kinetics, thereby improving the reversibility and efficiency of Li_2S deposition/dissolution. The diminished internal resistance further suggests that HEP/C@S facilitates more efficient charge transfer and electrolyte infiltration, which are critical for mitigating kinetic barriers in Li–S batteries.

To quantitatively compare the Li^+ migration capabilities of different catalysts, we systematically investigated the diffusion coefficients (D_{Li^+}) through CV measurements at varying scan rates (0.1–0.5 mV s^{-1}). Fig. 4a–d displays the CV profiles of cells incorporating HEP/C@S, MEP/C@S, Fe_2P/C@S, and Mn_2P/C@S cathodes, all exhibiting consistent electrochemical behavior across scan rates. Each CV curve features one distinct oxidation peak (peak A) and two characteristic reduction peaks (peaks B and C, corresponding to higher and lower potential processes, respectively). The linear relationship between peak currents and the square root of scan rates ($\nu^{1/2}$) was employed to evaluate Li^+ diffusion kinetics. As shown in Fig. 4e, HEP/C@S demonstrates significantly steeper slopes for all redox peaks (peak A: 212; peak B: 121; peak C: 105) compared to other catalysts, indicating its superior ability to facilitate Li^+ transport during polysulfide conversion. Notably, MEP/C@S exhibits comparable Li^+ migration enhancement to HEP/C@S, though with slightly reduced efficiency. This similarity suggests that the improved ionic diffusion in both materials originates primarily from lattice distortions within their crystal structures, which reconstruct the Li^+ diffusion pathways and create more favorable conduction networks.

The electrochemical impedance spectra (EIS) in Fig. 4f were analyzed to evaluate the charge-transfer resistance (R_{ct}) of the different catalysts, and the corresponding equivalent circuit diagrams are provided in Fig. S13. The Nyquist plots for all cathodes exhibit a characteristic semicircle in the high-frequency region, corresponding to R_{ct}, and a linear segment in the low-frequency region, associated with Li^+ diffusion. Notably, the HEP/C@S cathode demonstrates the smallest semicircle diameter, indicating the lowest R_{ct}, along with a steep low-frequency slope, suggesting rapid Li^+ diffusion. These observations imply that the HEP/C@S electrode, with its high density of active sites and superior electrical conductivity, facilitates efficient charge transfer and enhances Li^+ mobility,

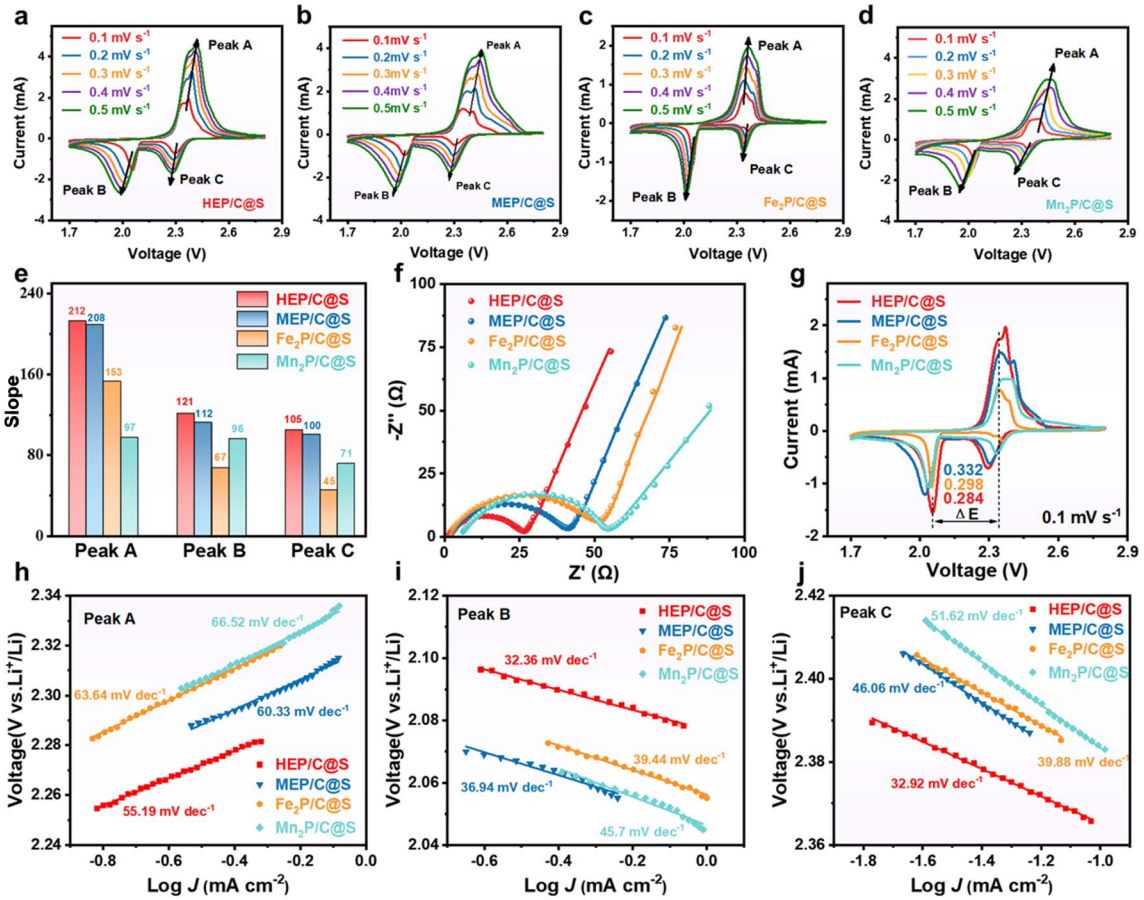

Fig. 4 CV curves of (a) HEP/C@S, (b) MEP/C@S, (c) Fe_2P/C@S, and (d) Mn_2P/C@S cathodes at sweep rates of 0.1, 0.2, 0.3, 0.4 and 0.5 mV s^{-1}, respectively. (e) The slopes of peaks A–C for each electrode in the bar chart. (f) Nyquist curves of HEP/C@S, MEP/C@S, Fe_2P/C@S, and Mn_2P/C@S. (g) The polarization potential between peaks A and B in the CV curves of various cathodes at sweep rates of 0.1 mV s^{-1}. Tafel plots of (h) peak A, (i) peak B, and (j) peak C.

thereby improving the kinetics of LiPS conversion and overall battery performance. In contrast, Mn_2P/C@S exhibits the largest R_{ct}, indicating poor electron transfer capability. This limitation significantly impedes the deposition of Li_2S, which is consistent with the earlier Gibbs free energy results.

Further electrochemical characterization was conducted *via* CV within a voltage window of 1.7–2.8 V at a scan rate of 0.1 mV s^{-1} (Fig. 4g). The HEP/C@S cathode exhibits significantly higher peak currents than the other tested materials, confirming its exceptional catalytic activity in promoting LiPS conversion. This enhancement arises from the synergistic interaction of LiPSs with the abundant active sites in HEP/C. Additionally, the polarization potential between redox peaks A and B was compared across cathodes. The HEP/C@S electrode displays the smallest ΔE (0.284 V), outperforming MEP/C@S (0.332 V), Fe_2P/C@S (0.298 V), and Mn_2P/C@S (0.311 V), indicating more facile sulfur redox reactions due to reduced kinetic barriers. Tafel analysis of the CV curves (Fig. 4h–j) reveals that the HEP/C@S cathode exhibits the lowest Tafel slopes for peaks A (55.19 mV dec^{-1}), B (32.36 mV dec^{-1}), and C (32.92 mV dec^{-1}), further corroborating its superior catalytic activity over the other materials. These results collectively demonstrate that the multi-metal-site structure of HEP/C significantly enhances LiPS conversion kinetics, making HEP/C@S a highly efficient sulfur host for Li–S batteries.

2.4 Electrochemical performance

Fig. 5a compares the initial charge–discharge profiles of Li–S batteries using HEP/C@S, MEP/C@S, Mn_2P/C@S, and Fe_2P/C@S cathodes at 0.2C current density within 1.7–2.8 V. The discharge curves exhibit two characteristic plateaus at approximately 2.30 V and 2.10 V, which correlate well with the cathodic reduction peaks observed in the CV measurements. These plateaus correspond to the sequential reduction of S_8 to soluble LiPSs and ultimately to insoluble Li_2S_2/Li_2S. Conversely, the charge profile shows a single plateau near 2.37 V, matching the anodic CV peak and representing the reverse oxidation process from Li_2S_2/Li_2S to LiPSs and eventually to S_8. As demonstrated in Fig. 5b, the HEP/C@S cathode displays superior electrochemical performance, manifested by the smallest polarization potential ($\Delta E = 150$ mV) among all tested materials (MEP/C@S: 210 mV; Mn_2P/C@S: 238 mV; Fe_2P/C@S: 290 mV). This reduced polarization indicates more efficient redox kinetics for LiPS conversion at the HEP/C@S interface. Furthermore, the ratio of

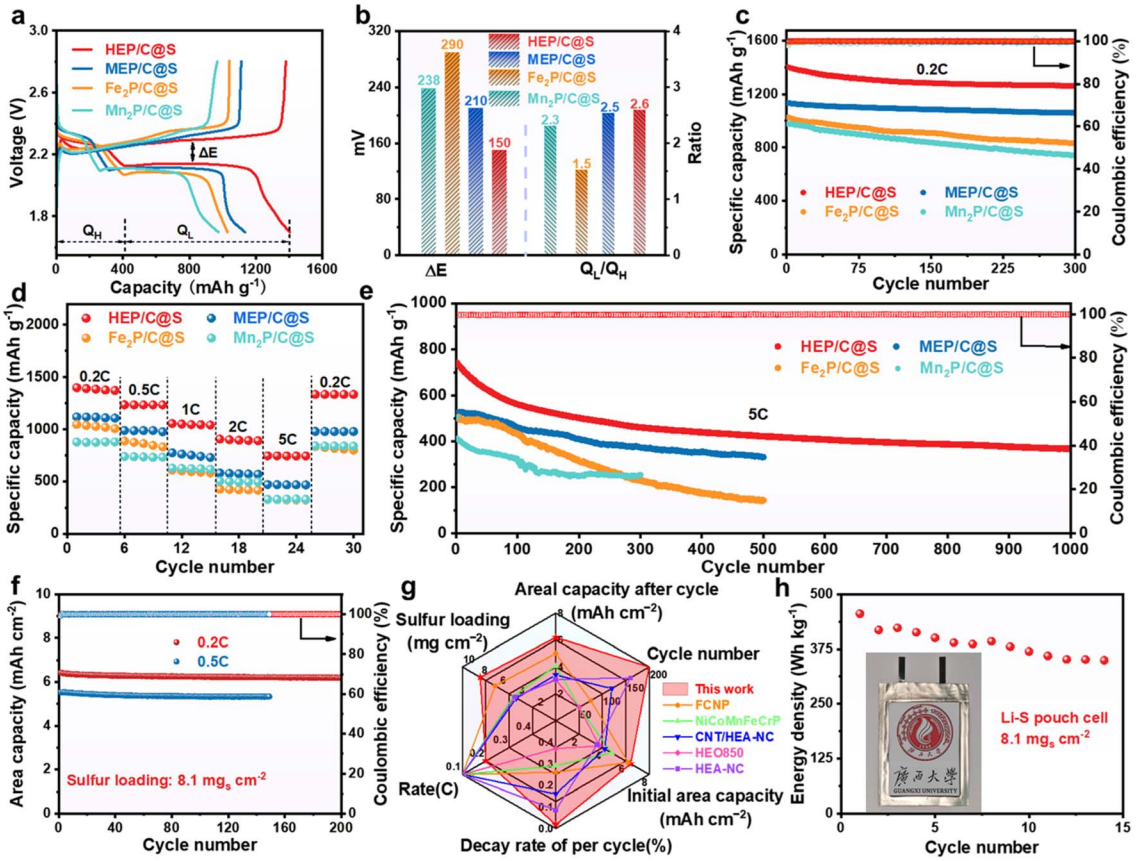

Fig. 5 (a) Charge/discharge profiles. (b) ΔE and Q_L/Q_H values obtained from the charge/discharge curves of the Li–S batteries. (c) Cycling performances at 0.2C, (d) rate performance at 0.2–5C, and (e) long-term cycling performance at 5C of HEP/C@S, MEP/C@S, Mn_2P/C@S and Fe_2P/C@S. (f) Cycling performances of HEP/C@S with sulfur loadings of 8.1 mg cm^{-2} at 0.2C and 0.5C. (g) Cycling performances of HEP/C@S under high sulfur loading with reported cathodes. (h) Cycling performance of an HEP/C@S||Li flexible Li–S pouch cell at 0.05C (inset: application of the HEP/C@S||Li flexible Li–S pouch cell).

discharge capacities from the lower to higher voltage plateaus (Q_L/Q_H) serves as a quantitative indicator of electrocatalytic activity toward polysulfide conversion. The HEP/C@S cathode achieves a remarkable Q_L/Q_H ratio of 2.6, outperforming MEP/C@S (2.5), Mn_2P/C@S (2.3), and Fe_2P/C@S (1.5). The outstanding performance of HEP/C@S can be ascribed to the synergistic catalytic effect arising from its five highly active metal sites. These sites collectively establish a low-energy-barrier pathway for LiPS redox reactions, significantly enhancing polysulfide conversion kinetics and overall battery performance.

Fig. 5c compares the long-term cycling stability of Li–S batteries with HEP/C@S, MEP/C@S, Mn_2P/C@S, and Fe_2P/C@S cathodes at 0.2C. The HEP/C@S cathode demonstrates superior performance, delivering an initial discharge capacity of 1402.1 mA h g^{-1}—significantly higher than those of MEP/C@S (1133.3 mA h g^{-1}), Mn_2P/C@S (978.4 mA h g^{-1}), and Fe_2P/C@S (1027.7 mA h g^{-1}). Moreover, after 300 cycles, HEP/C@S retains 1263.4 mA h g^{-1}, corresponding to a minimal capacity decay rate of 0.033% per cycle, outperforming the other cathodes in both capacity retention and cycling stability. The rate capability of these cathodes was further assessed at varying current densities (0.2–5C, Fig. 5d). The HEP/C@S cathode exhibits exceptional rate performance, delivering high discharge capacities of 1400.1, 1235.7, 1055.2, 906.6, and 745.7 mA h g^{-1} at 0.2, 0.5, 1, 2, and 5C, respectively. Notably, when the current density is restored to 0.2C, the capacity recovers to 1335.1 mA h g^{-1} (95.36% of its initial value), highlighting the electrode's structural robustness and efficient polysulfide conversion kinetics. Additionally, optical images of the lithium anode surfaces in lithium-sulfur batteries with different cathode materials were captured after 10 cycles at 0.2C (Fig. S14), demonstrating that the HEP/C@S cathode exhibits the best suppression of the shuttle effect. Even under high-rate cycling (5C, Fig. 5e), the HEP/C@S cathode maintains remarkable stability, providing an initial capacity of 740.7 mA h g^{-1} and retaining 367 mA h g^{-1} after 1000 cycles, with an ultralow decay rate of 0.05% per cycle. The control group material Fe_2P/C@S exhibits high capacity decay rates due to its poor adsorption capacity. Besides, MEP/C@S and Mn_2P/C@S show low cycling capacities because of their poor activation and promotion of S and LiPS conversion. As summarized in Table S1, HEP/C@S surpasses most previously reported cathode materials in terms of capacity, cycling life, and rate capability. These results

underscore the exceptional electrochemical properties of HEP/C@S, making it a highly promising cathode candidate for high-performance Li–S batteries.

To evaluate the practical viability of HEP/C, we assembled Li–S batteries with high sulfur loadings of 5.0–9.0 mg cm^{-2}. Remarkably, at a sulfur loading of 8.1 mg cm^{-2}, the HEP/C@S cathode delivered an initial areal capacity of 6.42 mA h cm^{-2} at 0.2C, maintaining 6.2 mA h cm^{-2} after 200 cycles with an exceptionally low capacity decay rate of 0.017% per cycle (Fig. 5f). Even under more demanding conditions (0.5C), the cathode demonstrated excellent stability, achieving an initial areal capacity of 5.53 mA h cm^{-2} and retaining 5.33 mA h cm^{-2} after 150 cycles with a decay rate of 0.024% per cycle. This indicates that a dual strategy involving adsorption and catalysis promises excellent electrochemical performance at high sulfur loading levels.[38,39] Comparative analysis (Fig. 5g) reveals that the electrochemical performance of HEP/C@S under high sulfur loading surpasses that of previously reported cathode materials, including FCNP,[40] NiCoMnFeCrP,[13] CNT/HEA-NC,[41] HEO850,[42] and HEA-NC.[43] Based on its excellent electrochemical performance at high sulfur loading, we fabricated a flexible Li–S pouch cell using the HEP/C@S cathode to further validate its practical utility for actual commercialization. The cell exhibited an open-circuit voltage of 3.13 V (Fig. S15) and, with an 8.1 mg cm^{-2} sulfur loading and E/S ratio of 10 : 1, delivered a high specific capacity of 1301.6 mA h g^{-1} and an outstanding energy density of 455.5 Wh kg^{-1} at 0.05C (Fig. 5h), which is comparable to that of state-of-the-art Li–S pouch cells in recent years.[44,45] The inset of Fig. 5h showcases the appearance of the pouch cell, highlighting its real-world applicability. These results collectively demonstrate the exceptional promise of HEP/C@S for next-generation, high-energy-density Li–S batteries.

3 Conclusions

In summary, we developed a facile one-step thermal synthesis strategy to fabricate single-phase high-entropy $Fe_{0.20}Co_{0.62}Ni_{0.14}Cu_{0.23}Mn_{0.38}P$ nanoparticles anchored on porous carbon networks (HEP/C), derived from cation (Fe^{3+}, Co^{2+}, Ni^{2+}, Cu^{2+} and Mn^{2+})-bonded phosphate resin precursors. As an efficient LiPS electrocatalyst in Li–S batteries, HEP/C significantly enhances LiPS redox kinetics and effectively suppresses the shuttle effect. DFT calculations reveal that the optimized d-band electronic structure of HEP enables strong LiPS adsorption and activation, while the synergistic interplay of multiple metal active sites facilitates efficient electron transfer and creates an optimal local chemical environment for LiPS conversion. The unique architecture of HEP/C provides abundant exposed catalytic sites, which not only significantly accelerate the LiPS conversion kinetics but also establish robust Li^+ diffusion channels. Consequently, the HEP/C@S cathode delivers a high specific capacity (1402.18 mA h g^{-1} at 0.2C), an outstanding cycling stability (0.05% capacity decay per cycle over 1000 cycles at 5C) and remarkable areal capacities (6.42 mA h cm^{-2} at 0.2C and 5.53 mA h cm^{-2} at 0.5C with 8.1 mg cm^{-2} sulfur loading). Additionally, a pouch cell with the HEP/C@S cathode exhibits a high initial energy density of 455 Wh kg^{-1}. This work not only presents a novel synthetic approach for high-entropy metal phosphides but also demonstrates their significant potential as high-efficiency electrocatalysts for practical high-performance Li–S battery applications.

Author contributions

Manchuan Guo and Jin Guo: writing – original draft, resources, methodology, formal analysis, data curation, conceptualization. Tao Ren and Haici Deng: data curation, software, writing – original draft. Yanqiu Zhu: writing – review & editing, supervision, project administration. Jinliang Zhu: writing – review & editing, writing – original draft, supervision, project administration, funding acquisition, formal analysis, conceptualization.

Conflicts of interest

The authors declare no conflict of interest.

Data availability

The data that support the findings of this article have been included as part of the SI.

Supplementary information: materials and instrumentation, detailed experimental procedures, additional characterization and electrochemical measurement. See DOI: **https://doi.org/10.1039/d5sc04604a**.

Acknowledgements

This work was supported by the Special Fund for Science and Technology Development of Guangxi (No. AD25069078), National Natural Science Foundation of China (52462027 and 51962002), and Innovation Project of Guangxi Graduate Education (YCSW2025031).

Notes and references

1 J. Xia, M. Lv, S. Zhang, Y. Xing and G. Zhou, *Mater. Sci. Eng., R*, 2025, **164**, 100985.
2 Z. Wang, J. Ke, H. Zhu, F. Xue, J. Jiang, W. Huang, M. Dong, X. Zhu, J. Zeng, R. Song, R. Sliz, Q. Ji, Q. Liu, Y. Fu and S. Lan, *Adv. Mater.*, 2025, **37**, 2504715.
3 R. Pai, A. Singh, M. H. Tang and V. Kalra, *Commun. Chem.*, 2022, **5**, 17.
4 Z. Wang, Y. Li, H. Ji, J. Zhou, T. Qian and C. Yan, *Adv. Mater.*, 2022, **34**, 2203699.
5 Y. Min, X. Zou, Q. Lu, W. Cai and Y. Bu, *Small*, 2025, **21**, 2411794.
6 Y. X. Li, Y. S. Feng, L. X. Li, X. Yin, F. F. Cao and H. Ye, *Energy Storage Mater.*, 2024, **67**, 103257.
7 R. He, S. Wang, L. Yang, S. Horta, Y. Ding, C. Di, X. Zhang, Y. Xu, M. Ibáñez, Y. Zhou, S. Mebs, H. Dau, J. N. Hausmann, W. Huo, P. W. Menezes and A. Cabot, *Energy Environ. Sci.*, 2024, **17**, 7193–7208.

8 B. Li, H. Wang, Y. Shen, Z. Zhang, Y. Xiong, M. Wang, W. Li, W. Zhou and J. He, *ACS Nano*, 2025, **19**, 12021–12032.
9 H. Raza, J. Cheng, J. Xu, L. An, J. Wang, W. Nie, G. Zheng and G. Chen, *Energy Environ. Mater.*, 2025, **8**, e70007.
10 H. Fan, Y. Si, Y. Zhang, F. Zhu, X. Wang and Y. Fu, *Green Energy Environ.*, 2024, **9**, 565–572.
11 W. Yang, T. Xu, C. Yang, H. Fan, W. Sun, X. Ma, X. Wang and Y. Fu, *Adv. Funct. Mater.*, 2024, **34**, 2409450.
12 R. Gao, Y. Zhang, P. Chen, T. Yan and X. Gao, *Adv. Funct. Mater.*, 2025, **35**, 2502090.
13 S. Liu, M. Chen, Y. Luo, Y. He, W. Zhang, Y. Chen, M. Wang, Y. Ye, K. Zhu, Y. Luo, R. Yu, J. Hou, H. Liu, H. Shu and X. Wang, *J. Colloid Interface. Sci.*, 2024, **669**, 126–136.
14 H. Jeong, Y. Park, Y. Lee, W. Jeong, H. Lee, G. Kim, G. Kim, H. Son and D.-H. Ha, *J. Mater. Chem. A*, 2025, **13**, 16995–17005.
15 X. Zhao, W. Sun, X. Liu, Z. Lu, K. Chen, J. Gao, J. Chen, H. Zhang and Z. Wen, *Adv. Energy Mater.*, 2025, **15**, 2404114.
16 W. Li, Y. Li, J.-H. Wang, S. Huang, A. Chen, L. Yang, J. Chen, L. He, W. K. Pang, L. Thomsen, B. Cowie, P. Xiong, Y. Zhou, G. Jang, D. H. Min, J. S. Byun, L. Xu, J.-Q. Huang, K. C. Roh, S. H. Kang, M. Liu, X. Duan and H. S. Park, *Energy Environ. Sci.*, 2024, **17**, 5387–5398.
17 X. Li, Z. Xie, S. Roy, L. Gao, J. Liu, B. Zhao, R. Wei, B. Tang, H. Wang, P. Ajayan and K. Tang, *Adv. Mater.*, 2025, **37**, 2410295.
18 Y. Zhou, L. Gao, H. Chen, H. Wang, J. Zhang, X. Li, F. Duo and G. Guan, *J. Mater. Sci. Technol.*, 2024, **168**, 62–70.
19 B. Zhang, M. Liu, J. Yin, W. Lu, P. Geng and W. Yi, *Int. J. Hydrogen Energy*, 2025, **105**, 521–530.
20 G. Cao, J. Liang, Z. Guo, K. Yang, G. Wang, H. Wang, X. Wan, Z. Li, Y. Bai, Y. Zhang, J. Liu, Y. Feng, Z. Zheng, C. Lu, G. He, Z. Xiong, Z. Liu, S. Chen, Y. Guo, M. Zeng, J. Lin and L. Fu, *Nature*, 2023, **619**, 73–77.
21 M. Gao, P. Gao, T. Lei, C. Ouyang, X. Wu, A. Wu and Y. Du, *J. Mater. Chem. A*, 2022, **10**, 15569–15579.
22 Y. Yang, J. Xia, X. Guan, Z. Wei, J. Yu, S. Zhang, Y. Xing and P. Yang, *Small*, 2022, **18**, 2204970.
23 Y. Xia, L. Guo, J. Zhu, J. Tang, Z. Li, X. Liu, J. Chi and L. Wang, *Appl. Catal., B*, 2024, **351**, 123995.
24 Y. Huang, W. Wu, M. Guo, X. Xu, X. Li, X. Liu and J. Zhu, *Sep. Purif. Technol.*, 2025, **356**, 129863.
25 K.-H. Kim, Y. S. Park, J. M. Lee, M. H. Seo, S.-H. Hong and S. M. Choi, *J. Mater. Chem. A*, 2025, **13**, 10111–10125.
26 W. Wu, X. Ma, Y. Zhu, F. Hu, G. Huang, N. Wang, S. Ning, Y. Zhu, P. Kang Shen and J. Zhu, *Chem. Eng. J.*, 2023, **478**, 147425.
27 X.-C. Liu, G. Wu, X. Han, Y. Wang, B. Wu, G. Wang, Y. Mu and X. Hong, *Adv. Mater.*, 2025, **37**, 2416749.
28 T. Zhang, Q. Liu, H. Bao, M. Wang, N. Wang, B. Zhang and H. J. Fan, *Nat. Commun.*, 2025, **16**, 1037.
29 X. Jiao, X. Tang, J. Li, Y. Xiang, C. Li, C. Tong, M. Shao and Z. Wei, *Chem. Sci.*, 2024, **15**, 7949–7964.
30 X. Li, Q. Guan, Z. Zhuang, Y. Zhang, Y. Lin, J. Wang, C. Shen, H. Lin, Y. Wang, L. Zhan and L. Ling, *ACS Nano*, 2023, **17**, 1653–1662.
31 P. Wang, B. Xi and S. Xiong, *Acc. Chem. Res.*, 2024, **57**, 2093–2104.
32 L. Xie, Y. Xiao, Q. Zeng, Y. Wang, J. Weng, H. Lu, J. Rong, J. Yang, C. Zheng, Q. Zhang and S. Huang, *ACS Nano*, 2024, **18**, 12820–12829.
33 C. Dong, C. Ma, C. Zhou, Y. Yu, J. Wang, K. Yu, C. Shen, J. Gu, K. Yan, A. Zheng, M. Gong, X. Xu and L. Mai, *Adv. Mater.*, 2024, **36**, 2407070.
34 H. Fang, W. Hou, C. Li, S. Li, F. Chu, X. Li, X. Zhang, L. Hou, C. Yuan and Y. Ma, *Chem. Sci.*, 2025, **16**, 8487–8500.
35 S. Li, L. Li, Y. Zhao, H. Yang, H. Tong, S. Fan, Z. Wang and W. Xu, *Energy Storage Mater.*, 2024, **70**, 103477.
36 C.-X. Zhao, X.-Y. Li, M. Zhao, Z.-X. Chen, Y.-W. Song, W.-J. Chen, J.-N. Liu, B. Wang, X.-Q. Zhang, C.-M. Chen, B.-Q. Li, J.-Q. Huang and Q. Zhang, *J. Am. Chem. Soc.*, 2021, **143**, 19865–19872.
37 F. Liang, Q. Deng, S. Ning, H. He, N. Wang, Y. Zhu and J. Zhu, *Adv. Sci.*, 2024, **11**, 2403391.
38 C. Zhou, C. Dong, W. Wang, Y. Tian, C. Shen, K. Yan, L. Mai and X. Xu, *Interdiscip. Mater.*, 2024, **3**, 306–315.
39 T. Wang, J. He, X.-B. Cheng, J. Zhu, B. Lu and Y. Wu, *ACS Energy Lett.*, 2023, **8**, 116–150.
40 Q. Yang, X. Wei, X. Cao, L. Chen, L. Song, L. Kong, W. Sun, K. Xie and Y. Song, *Chem. Eng. J.*, 2023, **452**, 139638.
41 Y. Ma, Y. Ren, D. Sun, B. Wang, H. Wu, H. Bian, J. Cao, X. Cao, F. Ding, J. Lu and X. Meng, *J. Mater. Sci. Technol.*, 2024, **188**, 98–104.
42 H. Raza, J. Cheng, C. Lin, S. Majumder, G. Zheng and G. Chen, *EcoMat*, 2023, **5**, e12324.
43 Z. Wang, H. Ge, S. Liu, G. Li and X. Gao, *Energy Environ. Mater.*, 2023, **6**, e12358.
44 S. Li, Z. Chen, J. Chen, X. Luo, X. Qiu and Y. Qian, *Adv. Energy Mater.*, 2025, **15**, 2405461.
45 M. Li, H. Liu, H. Li, D. Luan, Z. Liu and X. W. Lou, *Angew. Chem., Int. Ed.*, 2025, **64**, e202503174.